Surface mobility and impact of precursor dosing during atomic layer deposition of platinum: in situ monitoring of nucleation and island growth

Reference

J. Dendooven, M. Van Daele, E. Solano, R. K. Ramachandran, M. M. Minjauw, A. Resta, A. Vlad, Y. Garreau, A. Coati, G. Portale and C. Detavernier, Physical Chemistry Chemical Physics **22** (43), 24917-24933 (2020).

Full text (Publisher's DOI): https://doi.org/10.1039/D0CP03563G

PCCP
Physical Chemistry Chemical Physics

Accepted Manuscript

This article can be cited before page numbers have been issued, to do this please use: J. Dendooven, M. Van Daele, E. Solano, R. K. Ramachandran, M. M. Minjauw, A. Resta, A. vlad, Y. garreau, A. coati, G. Portale and C. Detavernier, *Phys. Chem. Chem. Phys.*, 2020, DOI: 10.1039/D0CP03563G.

ROYAL SOCIETY OF CHEMISTRY

rsc.li/pccp

View Article Online
DOI: 10.1039/D0CP03563G

Journal Name

ARTICLE TYPE

Cite this: DOI: 00.0000/xxxxxxxxxx

Surface mobility and impact of precursor dosing during atomic layer deposition of platinum: in situ monitoring of nucleation and island growth†

Jolien Dendooven,*[a] Michiel Van Daele,[a] Eduardo Solano,[b] Ranjith K. Ramachandran,[a] Matthias M. Minjauw,[a] Andrea Resta,[c] Alina Vlad,[c] Yves Garreau,[c,d] Alessandro Coati,[c] Giuseppe Portale,[e] and Christophe Detavernier[a]

Received Date
Accepted Date

DOI: 00.0000/xxxxxxxxxx

The increasing interest in atomic layer deposition (ALD) of Pt for the controlled synthesis of supported nanoparticles for catalysis demands an in-depth understanding of the nucleation controlled growth behaviour. We present an *in situ* investigation of Pt ALD on planar Si substrates, with native SiO_2, by means of X-ray fluorescence (XRF) and grazing incidence small-angle X-ray scattering (GISAXS), using a custom-built synchrotron-compatible high-vacuum ALD setup and focusing on the thermal Pt ALD process, comprising of $MeCpPtMe_3$ and O_2 gas at 300 °C. The evolution in key scattering features provides insights into the growth kinetics of Pt deposits from small nuclei to isolated islands and coalesced worm-like structures. An analysis approach is introduced to extract dynamic information on the average real space parameters, such as Pt cluster shape, size, and spacing. The results indicate a nucleation stage, followed by a diffusion-mediated particle growth regime that is marked by a decrease in average areal density and the formation of laterally elongated Pt clusters. Growth of the Pt nanoparticles is thus not only governed by the adsorption of Pt precursor molecules from the gas-phase and subsequent combustion of the ligands, but is largely determined by adsorption of migrating Pt species on the surface and diffusion-driven particle coalescence. Moreover, the influence of the Pt precursor dose on the particle nucleation and growth is investigated. It is found that the precursor dose influences the deposition rate (number of Pt atoms per cycle), while the particle morphology for a specific Pt loading is independent of the precursor dose used in the ALD process. Our results prove that combining *in situ* GISAXS and XRF provides an excellent experimental strategy to obtain new fundamental insights about the role of deposition parameters on the morphology of Pt ALD depositions. This knowledge is vital to improve control over the Pt nucleation stage and enable efficient synthesis of supported nanocatalysts.

1 Introduction

The deposition of Pt-group noble metals by atomic layer deposition (ALD) has gained increasing attention in the last decade.[1] ALD is a cyclical process that relies on sequential self-terminating gas-solid reactions to produce highly conformal nanocoatings.[2,3] Although ALD is traditionally perceived as a layer-by-layer technique, ALD processes for noble metals are often characterized by a nucleation-controlled growth on oxide surfaces. After a certain incubation period, growth is initiated in localized islands spread across the surface. This Volmer-Weber type island growth can be used advantageously for the deposition of noble metal nanoparticles, e.g. for applications in catalysis.[4–7] The increasing interest in ALD for depositing noble metal nanoparticles is mainly motivated by its unique ability to control the deposition process at the atomic level. Several authors have demonstrated nanoscale tuning of the size of the nanoparticles by changing the number of applied ALD cycles.[5,8–14] Moreover, by selecting the proper ALD process conditions, growth on oxide surfaces can be avoided and selective growth on metal surfaces can be achieved.[15–17] This offers opportunities to grow core/shell[15,17–19] and alloy[16,20] noble

[a] Department of Solid State Sciences, CoCooN group, Ghent University, Krijgslaan 281/S1, Belgium. E-mail: jolien.dendooven@ugent.be
[b] ALBA Synchrotron Light Source, NCD-SWEET beamline, Cerdanyola del Vallès, Spain.
[c] Synchrotron SOLEIL, SixS Beamline, L'Orme des Merisiers, Saint-Aubin, BP48, 91192 Gif-sur-Yvette, France.
[d] Université de Paris, CNRS, Laboratoire Matériaux et Phénoménes Quantiques, CNRS, F-75013 Paris, France.
[e] ESRF European Synchrotron, DUBBLE Beamline BM26, Avenue des Martyrs, CS40220, 38043 Grenoble, France; Present address: Macromolecular Chemistry & New Polymeric Materials, University of Groningen, Nijenborgh 4, AG Groningen, 9747, The Netherlands.

† Electronic Supplementary Information (ESI) available. See DOI: 00.0000/00000000.

View Article Online
DOI: 10.1039/D0CP03563G

metal nanoparticles by ALD as well as to develop novel bottom-up approaches for nanopatterning.[21] Not only the ALD process conditions play a crucial role but the substrate itself and pre-treatment steps can significantly influence the nucleation of the noble metal nanoparticles.[22–26]

Despite numerous reports on noble metal nanoparticle deposition by ALD, the mechanisms that govern the very initial stages of growth are still not fully understood. Surface processes such as diffusion of deposited atoms,[5,12,27–31] adsorption of precursor ligands on the substrate,[5,23,26,31–33] thermal decomposition of the metal precursor,[31,34,35] and reactions catalyzed by the deposited nanoparticles[5,31] are suggested to play a role. The kinetics of these processes are expected to vary with the noble metal loading and morphology and will therefore likely evolve during the ALD process.[5] Moreover, the nucleation and island growth mechanisms and kinetics are influenced by the choice of ALD process conditions, e.g. precursor/reactant type, exposure and deposition temperature, resulting in different incubation times and nanoparticles morphologies. Although some efforts have been made,[5,12,14,23,26,28,31,34,36] it is essential to further improve our understanding of the role of the different deposition parameters in order to enhance the control over the ALD technique for the tailored deposition of noble metal nanoparticles.

Most experimental studies concerning the nucleation of noble metal ALD are limited by the fact that they rely on the *ex situ* study of static morphologies alone, without providing detailed insights into how the structure evolves during the ALD process. The effect of a certain deposition parameter is, for example, typically studied by transmission electron microscopy (TEM) and a comparison of the nanoparticle size (distribution) is made for a specific number of ALD cycles. However, dynamic knowledge about how the nucleation and particle growth evolve during ALD for different process conditions is crucial to deepen our understanding of the underlying mechanisms and this can only be achieved by applying *in situ* probing techniques.

Grazing incidence small angle X-ray scattering (GISAXS) is a measurement technique typically performed at a synchrotron, that can yield information about the size, morphology and distribution of nanoscale objects at surfaces, which is averaged over the macroscopic surface area of the sample due to the large footprint of the beam.[37,38] Because no special sample preparation is required, GISAXS is ideally suited for a variety of *in situ* experiments, including the characterization of deposition processes in high vacuum.[39–43] As an illustration, the technique has been used for real-time monitoring of noble metal growth by evaporation[44–46] and sputtering.[47–50] In ALD-related research, *in situ* GISAXS has been used to study the initial growth of oxides, nitrides, and metals[12,51–56] and has been used to study the conformal coating of nanoporous thin films[57] and layers of quantum dots.[58] Besides monitoring the thin film growth, it is also possible to monitor the behaviour of a deposited film under several conditions, for example, sintering of Pt nanoparticles during annealing in different oxidizing atmospheres,[59] or the formation of bimetallic nanoparticles by annealing ALD deposited layers.[60]

A few reports presented *ex situ*[26,27,61–63] or *in situ*[12] GISAXS measurements during Pt ALD. In 2009, Christensen et al. investigated the morphology of Pt nanoparticles grown by 10, 20, 30 and 40 ALD cycles on $SrTiO_3$ surfaces.[27] The GISAXS patterns revealed an increase in center-to-center particle distance with increasing number of ALD cycles, suggesting that surface diffusion of Pt species influences the nanoparticle formation. In 2014, Geyer et al. recorded GISAXS patterns for a series of ALD-grown Pt nanoparticles on native SiO_2 surfaces.[62] Assuming a model in which the total island nucleation rate is kept constant, a lateral particle growth rate of 1 Å/cycle was extracted. More recently, *in situ* GISAXS measurements during Pt ALD revealed that the particle size and coverage can be tuned by either utilizing O_2 or N_2 plasma as the co-reactant.[12]

In this paper, we present findings from the use of GISAXS to monitor *in situ* Pt ALD growth and highlight its suitability to probe surface mobility during nanoparticle ALD. Results are shown for the Pt ALD process using $MeCpPtMe_3$ and O_2 gas at 300 °C, which is considered a model system for the O_2-based noble metal ALD processes.[64] Combining synchrotron radiation and a dedicated ALD setup we can resolve the dynamics of Pt particle formation and growth. In addition to the *in situ* morphological characterization by GISAXS, *in situ* X-ray fluorescence (XRF) was used to quantify the amount of Pt atoms on the surface. An analysis strategy is introduced to correlate the amount of deposited material with the evolution of structural parameters such as Pt cluster shape, average size and areal density. The presented experimental approach enables the detailed investigation of the influence of different processing conditions on the nucleation and island growth mode during Pt metal ALD, which could be extended to other noble metal ALD processes. As a proof of concept we investigate the influence of the $MeCpPtMe_3$ precursor pressure on the morphology of the deposited Pt particles.

2 Experimental Section

2.1 Transportable setup for *in situ* investigation of ALD with synchrotron radiation

A drawing and picture of the custom-built synchrotron-compatible ALD setup, used in this work, are shown in Figure 1.[56] The setup consists of a stainless steel chamber equipped with a turbo pump and rotary vane backing pump, enabling a base pressure of 10^{-6} mbar. The main ALD components include a flange with heated sample stage, computer-controlled gas inlet valves and a remote RF plasma source. The setup can be transported and installed at synchrotron beamlines, in particular on the MED diffractometer with hexapod of the SixS beamline at the SOLEIL synchrotron facility and on the Huber goniometer of the DUBBLE BM26B beamline at the ESRF synchrotron facility. The chamber is equipped with three Be windows, allowing exposure of the sample to an intense monochromatic X-ray beam and detection of the scattered and fluorescent radiation from the sample. For *in situ* GISAXS studies, the setup is expanded with motorized anti-scattering slits that can be positioned close to the path of the X-ray beam to eliminate unwanted scattered X-rays. This is obtained by placing tungsten slits and a knife edge inside the vacuum, right after the entrance Be window. Right before the exit Be window a tungsten rod-like beamstop is placed in-vacuum to largely

View Article Online
DOI: 10.1039/D0CP03563G

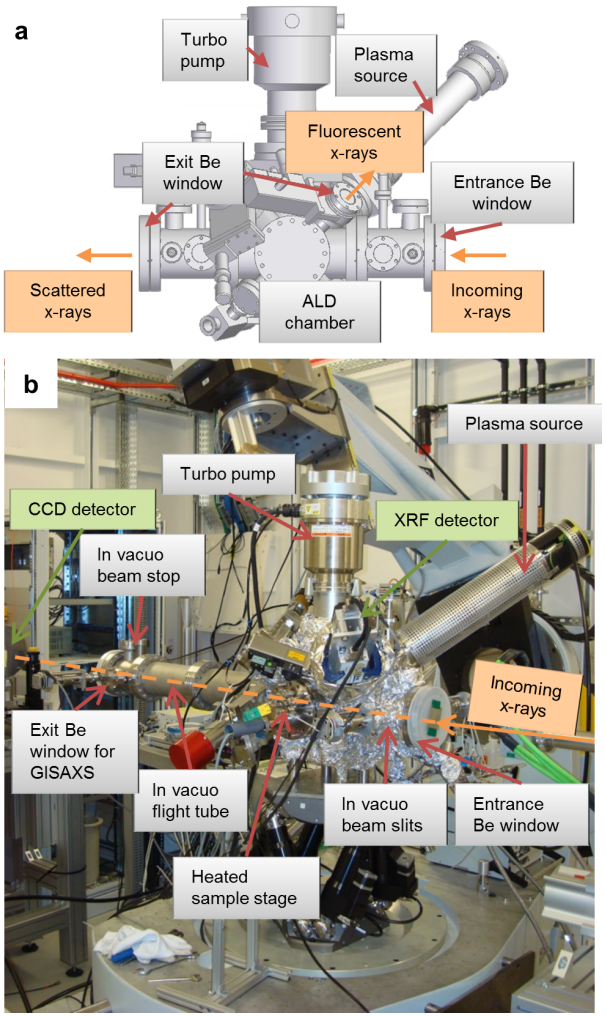

Fig. 1 (a) Drawing of the transportable synchrotron-compatible high-vacuum ALD setup, dedicated for *in situ* XRF and GISAXS measurements during ALD. (b) Picture of the setup, installed at the SixS beamline of the SOLEIL synchrotron facility.

block the intense direct and specular reflected X-ray beams, thus suppressing background scattering from the exit window. Precise alignment and rotation of the sample relative to the incoming X-ray beam is enabled by the aforementioned positioning devices that are available at the SixS (SOLEIL) and DUBBLE BM26B (ESRF) beamlines.

2.2 Substrate preparation and ALD of Pt

Si wafers with native SiO_2 are used as substrates. Prior to ALD growth, the substrate and support are heated to 300 °C and exposed to a remote O_2 plasma (10 s, 1.2×10^{-3} mbar, at 200 W) to clean the sample surface and improve reproducibility between the different experiments. ALD of Pt is conducted at 300 °C using $MeCpPtMe_3$ (Strem Chemicals, 99 %) and O_2 gas. The Pt precursor is kept in a stainless steel container heated to 30 °C and Ar is used as a carrier gas. Unless stated otherwise, a static exposure mode is applied, meaning that the valves to the pumping system are closed during exposure of the sample to the Pt precursor or to O_2 gas. The other precursor exposure mode that is used is a pump exposure mode, during which the valves to the pumping system are kept open during the exposure. For both static and pump exposure modes the precursor exposure time is 15 s, the precursor pumping time is 30 s, the O_2 exposure time is 10 s, and the O_2 pumping time is 15 s. The pressure in the chamber during the static precursor exposure reaches ~1 mbar, during the pump precursor exposure it is $\sim6\times10^{-3}$ mbar, and ~1 mbar during the O_2 exposure.

2.3 GISAXS geometry

A schematic representation of the GISAXS experiment is shown in Figure 2. The X-ray beam hits the sample under a grazing angle (α_i) and is scattered by the ensemble of Pt nanoparticles on the surface. The scattered intensity as a function of the exit angles α_f and $2\theta_f$ is recorded by a 2D area detector. The angular coordinates of the detector are related to the wavevector transfer ($\mathbf{q} = \mathbf{k_f} - \mathbf{k_i}$) and the detector plane is converted to reciprocal q-space coordinates using the equations: $q_y = (2\pi/\lambda)sin(2\theta_f)cos(\alpha_f)$ and $q_z = (2\pi/\lambda)(sin(\alpha_i)+sin(\alpha_f))$ with q_y and q_z the scattering vector components parallel and perpendicular to the sample surface, respectively. The $q_x = (2\pi/\lambda)(cos(2\theta_f)cos(\alpha_f) - cos(\alpha_i))$ scattering vector component has a very low value due to the low incident and exit angles that are used in GISAXS and can be neglected. The scattered intensity $I(\mathbf{q})$ is modulated by the form factor $F(\mathbf{q})$ and the structure factor $S(\mathbf{q})$, describing the scattering contribution from the particle shape and organization of the nanoparticles, respectively. The key features that are observed in the scattering pattern are directly linked to the real-space morphology of the nanoparticles ensemble. Intensity modulations along the q_z direction contain information about dimensions perpendicular to the sample surface, such as the particle height. Modulations along the q_y direction contain information about average lateral dimensions, such as the particle width and center-to-center distance between neighbouring nanoparticles. Another scattering feature is the Yoneda (or Vineyard) peak, i.e. an enhancement of the scattered intensity for the exit angle α_f that is equal to the critical angle of the sample α_c. Therefore, the dependence of the Yoneda peak on the optical surface properties provides information about the surface composition.

2.4 *In situ* XRF and GISAXS measurements

In situ XRF and GISAXS measurements during ALD were performed at the SixS (SOLEIL) and DUBBLE BM26B (ESRF) beamlines. To avoid decomposition of the Pt precursor by the X-rays, the sample is only illuminated after the reactor is pumped to base pressure. Samples were exposed to the X-rays after every second ALD cycle and a fluorescence spectrum and scattering pattern are recorded. To enable excitation of the Pt Lα emission lines for XRF, the X-ray energy is set to 12 keV, which is slightly above the L3 absorption edge of Pt at 11.56 keV. An incidence angle of 1.2° was used for XRF measurements, each spectrum was acquired in 30 s with an energy-dispersive silicon drift detector (Röntek and Vortex at SixS (SOLEIL) and DUBBLE BM26B (ESRF), respectively). GISAXS patterns were recorded at an incidence angle of 0.5°, which is well above the critical angle of Pt (α_c = 0.38°, at

View Article Online
DOI: 10.1039/D0CP03563G

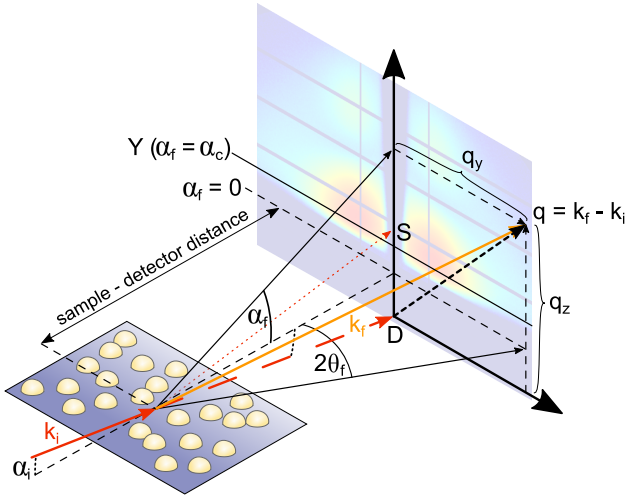

Fig. 2 Schematic representation of the GISAXS geometry. A monochromatic X-ray beam hits the sample at an incidence angle α_i. The exit angles of the scattered beam are denoted by α_f and $2\theta_f$. The position of the direct beam D (at $\alpha_f = -\alpha_i$) marks the origin for the q_y and q_z components of the scattering vector. The specular reflected beam S (at $\alpha_f = \alpha_i$) is masked by a rod-shaped beamstop, placed in vacuum between the sample and exit Be window. The Yoneda peak (Y) is observed at the critical angle of the sample ($\alpha_f = \alpha_c$).

12 keV). Firstly, this ensures full penetration of the Pt layer and, secondly, a clear separation of the Pt Yoneda peak and the specular peak in the scattering pattern. The sample-detector distance was calibrated with a silver behenate sample.

At the SixS (SOLEIL) beamline, the X-ray beam at the sample position was 0.3 mm × 0.4 mm (horizontal and vertical, respectively) and the 2D GISAXS patterns were acquired with a MarCCD detector (2048×2048 pixels, each pixel has a size of 80×80 μm^2) using a counting time of 20 s during the pumping step. The detector was positioned roughly 1.7 m from the sample. The in-vacuum flight tube was used to reduce background scattering and absorption from air. In addition to the in-vacuum beamstop, a lead strip was placed after the window to completely shield the detector from the intense direct beam and the scattered radiation from the exit Be window.

At the DUBBLE (ESRF) beamline, the X-ray beam was focused at the detector position, which results in a beam size of 1.0 mm × 0.4 mm (horizontal and vertical, respectively) at the sample position. The GISAXS patterns were acquired with a Dectris Pilatus 1M detector (981×1043 pixels H×V, each pixel having a size of 172×172 μm^2) using a counting time of 30 s during the pumping step and a sample-detector distance of 4.4 m was used. The pathway between the exit Be window of the ALD chamber and the detector was mostly evacuated by using a pumped flight tube with entrance and exit Kapton windows. A second beamstop was installed in front of the detector at the position of the direct and specular beam to prevent detector saturation and damage.

2.5 GISAXS data analysis

In this work, we introduce an analysis approach, based on a geometrical model, to extract average real space parameters such as the Pt nanoparticle shape, size, and areal density from the q-space scattering data. To validate the proposed strategy, the measured GISAXS data were compared to simulated 2D GISAXS patterns that were calculated with the IsGISAXS software,[65] using the extracted morphological parameters as input for the simulation. The best agreement between simulation and data was obtained when two particle shapes in a 1:1 ratio were taken into account, being full spheroids and hemispheroids. Both particle geometries were described by the same particle height and radius. A lognormal distribution function was selected for the particle radius, and the distribution width was described by the geometric standard deviation σ. A joint distribution for the particle height was implemented in IsGISAXS assuming a Gaussian distribution for the particle aspect ratio height/radius, the distribution width being described by 0.05 times the central particle aspect ratio value. The distorted-wave Born approximation (DWBA) was used to calculate the form factor, the model of the graded interface was used to describe the perturbations caused by densely packed particles on a surface.[44] The calculations furthermore use the local monodisperse approximation (LMA) formalism, which is commonly used for polydispersed systems. A 1D paracrystal model was used to calculate the structure factor, which is a regular 1D lattice with loss of long-range order. A Gaussian function with disorder parameter ω, calculated as ω = 0.4×D described the distribution of the center-to-center distance D. Supplementary Figure 1 shows the most relevant parameters in the input file for the IsGISAXS software.

2.6 Complementary SEM and XRR measurements

The GISAXS data analysis approach is corroborated by *ex situ* X-ray reflectivity (XRR) and scanning electron microscopy (SEM) measurements. XRR is performed in a Bruker D8 system, equipped with a Cu Kα source and a point detector. SEM is performed in a FEI Quanta 200F instrument.

3 Results

3.1 *In situ* XRF: growth curve

XRF and GISAXS data was acquired after every two ALD cycles during Pt deposition. The integrated Pt L_α emission line was calibrated using Rutherford backscattering spectrometry (RBS).[12] This allows the determination of the Pt surface density as a function of the intensity of the Pt L_α signal, depicted as a function of the number of ALD cycles in Figure 3a. During the first ALD cycles (0 to 12) a slow growth regime was observed and a theoretical monolayer (TML) of Pt was obtained after 10 ALD cycles, indicating that the XRF setup is sensitive enough to detect a sub-monolayer surface coverage of Pt atoms. After the first slow growth a constant growth regime is quickly obtained (~26 ALD cycles) and after roughly 80 cycles the growth per cycle decreases to a lower value. The growth curve has an elongated S-shape, indicative of Pt nucleation followed by particle growth and coalescence.[66,67]

Additional samples with selected Pt surface densities (marked points 1-4) were prepared and measured by *ex situ* SEM. The obtained SEM micrographs (Figure 3b) provide snapshots of the par-

View Article Online
DOI: 10.1039/D0CP03563G

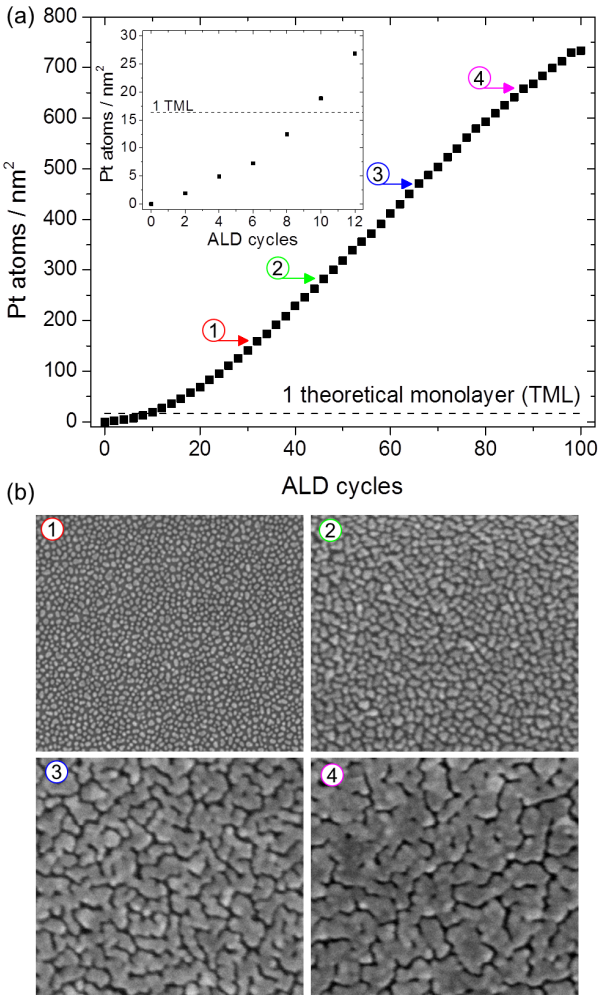

Fig. 3 (a) RBS-calibrated *in situ* XRF data: surface density of Pt atoms as a function of the number of ALD cycles. The inset shows a detail of the nucleation stage during the first 12 ALD cycles. (b) SEM images for selected Pt loadings: (1) ~ 160, (2) ~ 280, (3) ~ 470, (4) ~ 660 Pt atoms per nm^2. Each SEM image is 500 nm wide.

ticle morphology and distribution at different Pt surface densities (i.e. different ALD cycles). The SEM micrograph of the low Pt surface density (~160 atoms/nm^2, Figure 3b(1)) indicates that the Pt nucleates, and forms particles, on the SiO_2 surface. The other SEM micrographs indicate that after the particles are formed they increase in size and start to coalesce (2), forming larger and more irregular particle shapes. They continue growing and merging, resulting into even larger worm-like structures (3) and finally start to form a percolating Pt layer across the substrate when the Pt loading is high enough (4). For even higher Pt surface densities the slope of the growth curve decreases, indicating that the available surface area for precursor adsorption starts to decrease after percolation.

3.2 *In situ* GISAXS: particle nucleation

The Pt nucleation stage on native SiO_2 was investigated using *in situ* 2D GISAXS measurements. The GISAXS scattering patterns that were recorded during the first 12 ALD cycles are displayed in Figure 4a. After the first ALD cycles there is an increase of the background scattering intensity in the pattern ($q_y \neq 0\,nm^{-1}$). Additional ALD cycles cause the scattering intensity to increase further and make it clear that a single scattering peak is present in the pattern. This indicates that there are correlated Pt clusters distributed on the surface during the nucleation stage. To study the evolution of the scattering peak along the q_y direction, horizontal cuts were taken at the q_z position of maximum intensity (Yoneda peak) and are depicted in Figure 4b. Fits with Lorentzian functions were performed for all but the first cut (0 ALD cycles) and are displayed as the black lines, overlapping the data. From these cuts it is clear that an off-specular scattering signal is already present after 2 ALD cycles, with the maximum scattering intensity observed at $q_y = 0.59\,nm^{-1}$, indicating that Pt clusters were already present on the surface. Additional ALD cycles result in an increase in intensity and shifts in the q_y position of maximum intensity of the scattering peak.

The q_y maximum of the scattering peak ($q_{y,max}$) can be approximated to the mean center-to-center distance (D) between scattering centra by using: $D = 2\pi/q_{y,max}$.[37] Therefore, lower $q_{y,max}$ values are related to larger mean center-to-center distances and *vice versa*. The $q_{y,max}$ value for each horizontal cut is obtained from a fit through the data and these are plotted (with a 95 % confidence interval) as a function of the number of ALD cycles and Pt surface density in Figure 4c. The inset shows the $q_{y,max}$ values converted from q-space to real space values (D). The $q_{y,max}$ position shows a considerable shift towards higher values during the first 6 ALD cycles, which indicates a decrease for the mean particle distance and a rise in the number of deposited nuclei on the surface. New nuclei are deposited between the existing clusters until a critical or saturated coverage is reached, giving an estimated saturated particle density of N~1.8×10^{12} nuclei/cm^2 (N~D^{-2}) after 6 ALD cycles. This value for the particle density corresponds with particle densities that can be expected for metal particles on an oxide surface (10^{12}-10^{13} nuclei/cm^2) in literature.[5,68] Additional ALD cycles result in a gradual shift of the $q_{y,max}$ position towards lower q_y values, showing an increase in the particle center-to-center dis-

View Article Online
DOI: 10.1039/D0CP03563G

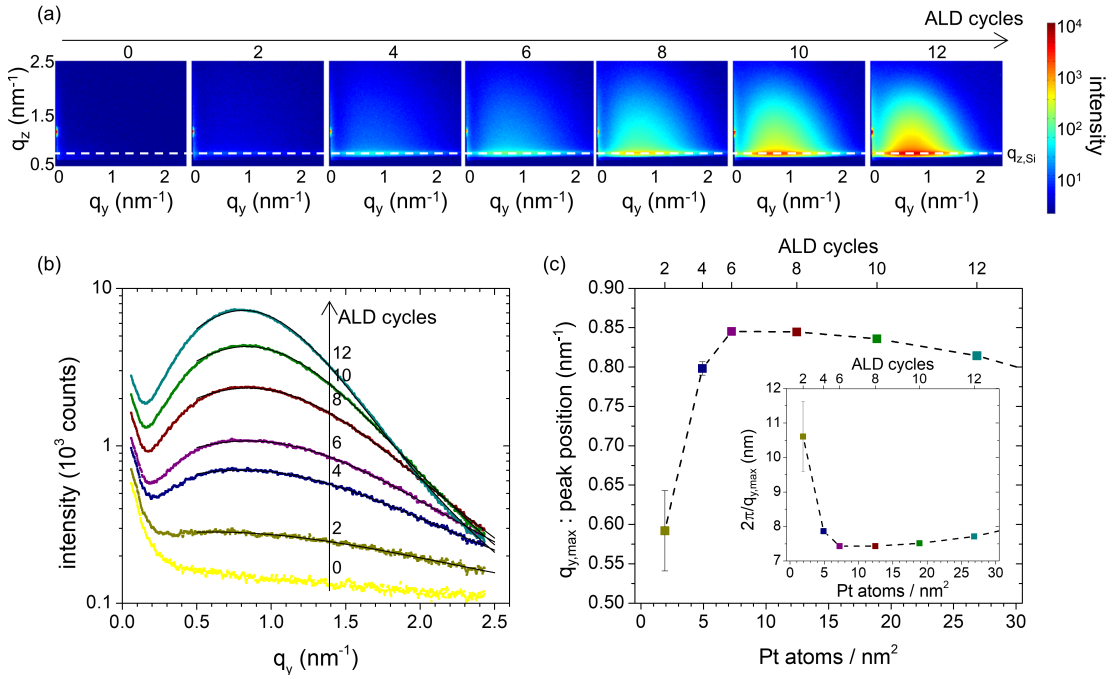

Fig. 4 (a) *In situ* GISAXS patterns measured during the nucleation stage. The dashed white line marks the position of the Si Yoneda. (b) Horizontal line profiles are taken at the q_z position of maximum intensity, which correspond to the Si Yoneda position. The black lines are fits to the data points. (c) The peak position, $q_{y,max}$ of the horizontal cuts as a function of the number of ALD cycles (top x-axis) and the surface density of Pt atoms (bottom x-axis). The peak positions were obtained from the fits shown in (b). The inset shows the values which correspond to: $2\pi/q_{y,max}$. The error bars represent the 95 % confidence intervals for the fitted $q_{y,max}$ values

tance and indicates a reduction in the number of scattering nuclei due to coalescence. Surface diffusion will rather result in the growth of existing islands instead of the formation of a new stable nucleus.

3.3 *In situ* GISAXS: particle growth and coalescence

After the nucleation stage the Pt ALD process exhibits enhanced growth behaviour until layer closure starts to occur, see the *in situ* XRF curve (Figure 3a). This intermediate stage was also investigated during the ALD process. Figure 5 displays selected *in situ* 2D GISAXS patterns with Pt surface densities (Pt loading) that correspond to the marked points on the *in situ* XRF curve and the *ex situ* SEM micrographs, shown in Figure 3. The GISAXS patterns show that the main scattering peak increases in intensity as a function of the Pt loading and that the position of the maximum shifts to lower q_y values and higher q_z values. The shift in q_y to lower values indicates an increase in the mean center-to-center particle distance with higher Pt loadings due to nanoparticle coalescence. The q_z position of maximum scattering intensity (Yoneda peak) depends on the critical angle of the scattering surface and is therefore dependent on the material density of the scattering volume. The dashed white lines in Figure 5 mark the expected Yoneda positions for a Si and Pt surface. It is clear that the Yoneda peak in the pattern starts at the position for a Si surface, as expected by the low Pt loading on the surface. Increasing the Pt loading results in a shift of the Yoneda peak position towards the expected value of Pt, due to the fact that the average density of the scattering volume increases with Pt loading. Both

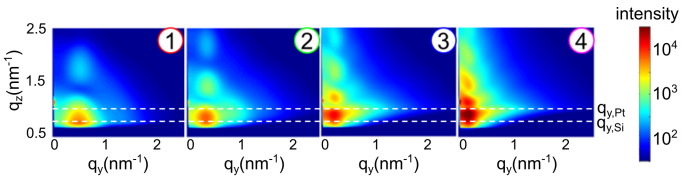

Fig. 5 *In situ* GISAXS patterns measured during the growth and coalescence stage of the Pt ALD process. The selected patterns correspond to (1) 32, (2) 46, (3) 66, (4) 88 ALD cycles and a Pt surface density of (1) 160, (2) 280, (3) 470, (4) 660 atoms per nm^2. The Si and Pt Yoneda positions are indicated by the dashed white lines.

shifts in the position of the main scattering peak are consistent with the growth and coalescence behaviour of the Pt particles, as seen in the *ex situ* SEM micrographs (Figure 3b). In addition to the shift of the main scattering peak, secondary scattering maxima and minima appear above the main peak with increasing Pt loading and shift towards lower q_z values. This indicates that the mean particle height increases as a function of the Pt loading. Finally, the arc-like features that can be observed in the out-of-plane scattering recorded at ALD cycles 32 and 46 (respectively, patterns 1 and 2 in Figure 5) can be associated with a spheroidal particle shape. [12,48]

Figure 5 shows the 2D scattering patterns for selected Pt loadings, which allows for a quick qualitative assessment of the surface morphology. However, further analysis is required to obtain quantitative information about the evolution of the scattering features as a function of the Pt surface density. As a first step towards quantitative analysis, horizontal and vertical cuts were taken and

View Article Online
DOI: 10.1039/D0CP03563G

plotted in a 2D colour map as a function of the Pt surface density.

The horizontal cuts were taken at the q_z position of maximum intensity of the main scattering peak and are shown in Figure 6a. The solid black line indicates the evolution of the first maximum and its data points are displayed in Figure 6b. As detailed in Figure 4c, the $q_{y,max}$ position starts around 0.6 nm^{-1}, increases during the first 6 ALD cycles to 0.85 nm^{-1}, and then smoothly shifts to lower values. The $q_{y,max}$ position is related to the mean center-to-center distance between the Pt particles and the corresponding real space value is shown in the insert of Figure 6b. This again shows that after an initial decrease of the inter-particle distance it gradually increases, indicating that after nucleation and reaching the saturated particle coverage the scattering centra are spaced further apart with every consecutive ALD cycle, due to coalescence of the Pt particles.

A second scattering feature appears after roughly 22 cycles (~80 Pt atoms/nm^2) and upon its appearance gradually shifts to lower q_y values. This behaviour is also present for the minimum position between both maxima, as can be seen in Figure 6c and by the dashed line in Figure 6a. This minimum is a feature of the form factor of the particles. As the horizontal scattering features give information about the in-plane dimensions the change in the position of this minimum is related to the size of the particles and can be used to deduce an approximate value for the mean particle radius. Simulations of the form factor of full spheroids and hemi-spheroids with a range of relevant particle widths and heights were performed to obtain a relation between the $q_{y,min}$ value and the particle radius, which gave the following relation: radius = $4.4/q_{y,min}$ (see Supporting Information). The estimated values for the particle radius are displayed in the insert of Figure 6c. This shows that the mean radius of the particles keeps increasing as a function of the Pt loading, which is to be expected from the *ex situ* SEM images. The coloured numbers and arrows correspond to Pt loadings that are marked on the XRF curve and the SEM micrographs in Figure 3.

The vertical cuts were taken at the q_y position of maximum intensity for the main scattering peak and are shown in Figure 7a; the Si and Pt Yoneda positions are marked. The evolution in q_z position of the main scattering peak is displayed in Figure 7b. It is clear that the maximum intensity in q_z starts at the position for the Si Yoneda and by increasing the Pt loading it shifts towards the position that is expected for a bulk Pt surface, showing an abrupt transition around a surface density of 250 Pt atoms per nm^2. Comparing the *ex situ* SEM micrographs (Figure 3b) before (1) and after (2) this transition show a large difference in morphology for the Pt particles. Before the transition (Figure 3b-1) the particles can still be considered isolated and isotropic in shape. After the transition (Figure 3b-2) the particles are merging and form elongated, worm-like structures. The abrupt shift in the $q_{z,max}$ position seems to coincide with a change in the morphology of the Pt particles. For high Pt loadings, the SEM micrographs reveal a morphology that can be considered as a Pt thin film with gap-like voids.

After a few ALD cycles secondary vertical scattering maxima appear, marked in Figure 7a by the solid black lines. The minima between two adjacent maxima are marked by the dashed black

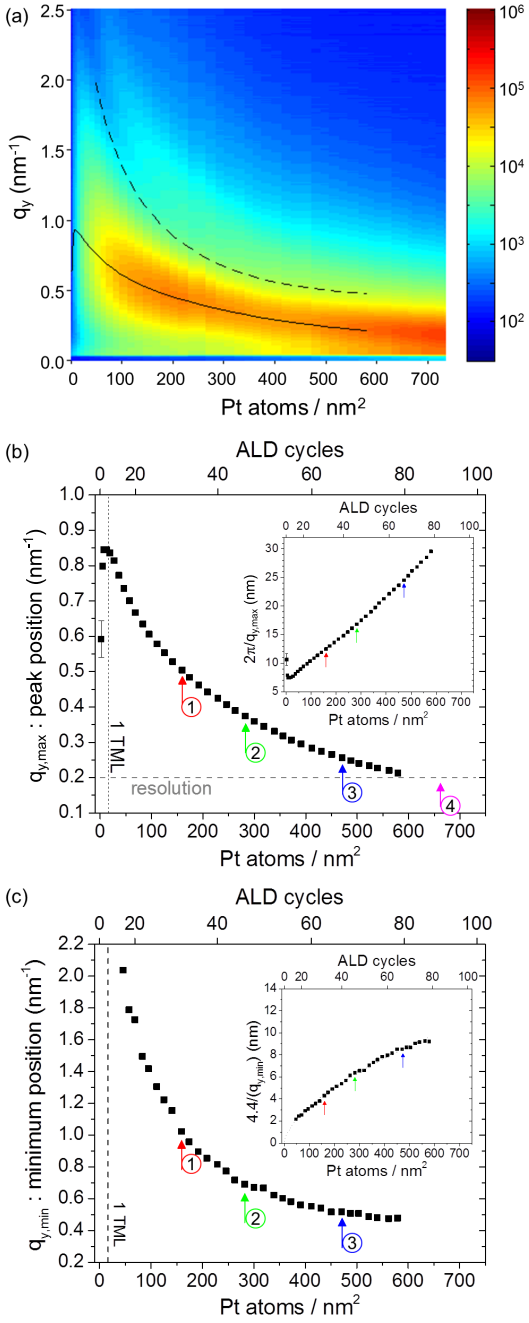

Fig. 6 (a) Intensity evolution of the horizontal line profiles as a function of Pt surface density. The horizontal cuts were taken at the q_z position of maximum intensity of the main scattering peak. The q_y positions of the first maximum and minimum are indicated by the solid and dashed black lines, respectively. (b) $q_{y,max}$ position of the first maximum versus ALD cycles (top x-axis) and Pt surface density (bottom x-axis). The corresponding $2\pi/q_{y,max}$ values are shown in the insert. (c) $q_{y,min}$ position of the first minimum versus ALD cycles and Pt surface density. The corresponding estimated mean particle radius values ($4.4/q_{y,min}$) are shown in the insert. The coloured numbers and arrows correspond to the marked points in Figure 3.

View Article Online
DOI: 10.1039/D0CP03563G

lines. These maxima gradually shift towards lower q_z positions with increasing Pt surface density, indicating that the deposited Pt particles are increasing in height. The average distance between two adjacent maxima or minima is taken and plotted in Figure 7c. By using the approximation $H = 2\pi/ < \Delta q_z >$ it is possible to estimate the mean height (H) of the deposited film, the corresponding values are shown in the inset of Figure 7c. Based on these results the obtained final thickness of the Pt layer was ~13 nm.

After 100 ALD cycles the deposition was stopped and the sample was characterized using X-ray reflectivity (XRR) and SEM, see Figure 8. The SEM image shows the worm-like structure of the deposited Pt layer. A thickness of 12.1 nm and roughness of 1.2 nm was obtained from the XRR fit, matching closely with the calculated final thickness from the GISAXS measurements (Figure 7c).

3.4 Strategy for analysing the GISAXS patterns

3.4.1 Geometrical model for "fast analysis" of GISAXS patterns

As outlined in the previous section, estimations for the mean particle height and width, and mean inter-particle distance can be deduced by evaluating the minima and maxima in the horizontal and vertical line profiles taken at the maximum intensity of the 2D GISAXS patterns. This approach is considered a "rapid" or "fast" data analysis.[37] Inspired by the work of Schwartzkopf et al.[48], we use this "fast" analysis as a basis for a simplified geometrical model that captures the essential parameters of the particle morphology on the sample, such as the average particle height, radius, and center-to-center distance, and is accurate enough to quickly determine changes in the morphology of the Pt particles during the initial stages of the ALD process, i.e. before agglomeration leads to wormlike features. In this model, the particles are modelled as full spheroids, without size distribution, on a regular 2D lattice. The average particle dimensions are derived from the above mentioned "fast" data analysis, i.e. the average particle height ($H = 2\pi/\Delta q_z$) and radius ($R = 4.4/q_{y,min}$), but takes into account a deviation for the inter-particle spacing based on the *in situ* recorded XRF data. Indeed, while a common approach to estimate the center-to-center distance D is to use the approximation $D = 2\pi/q_{y,max}$, often large discrepancies are observed with values obtained from real space TEM imaging, because the GISAXS intensity is governed by the interplay between the interference function and the form factor. Due to the latter, the observed $q_{y,max}$ peak position does not exactly correspond to the maximum of the interference function. The limitations of the approximation $D = 2\pi/q_{y,max}$ in our data become clear in Figure 9b, where the Pt surface density is calculated based on the estimated values for the average particle height, radius, and center-to-center distance. The mismatch between the measured Pt surface density by XRF (black squares) and the calculated Pt surface density with the geometrical model (open circles) can be attributed to a deviation in the estimated value of the center-to-center distance from its real value. Therefore, an alternative approach was developed, for which the XRF Pt surface density is used as the input for calculating the value of the center-to-center distance. In this approach

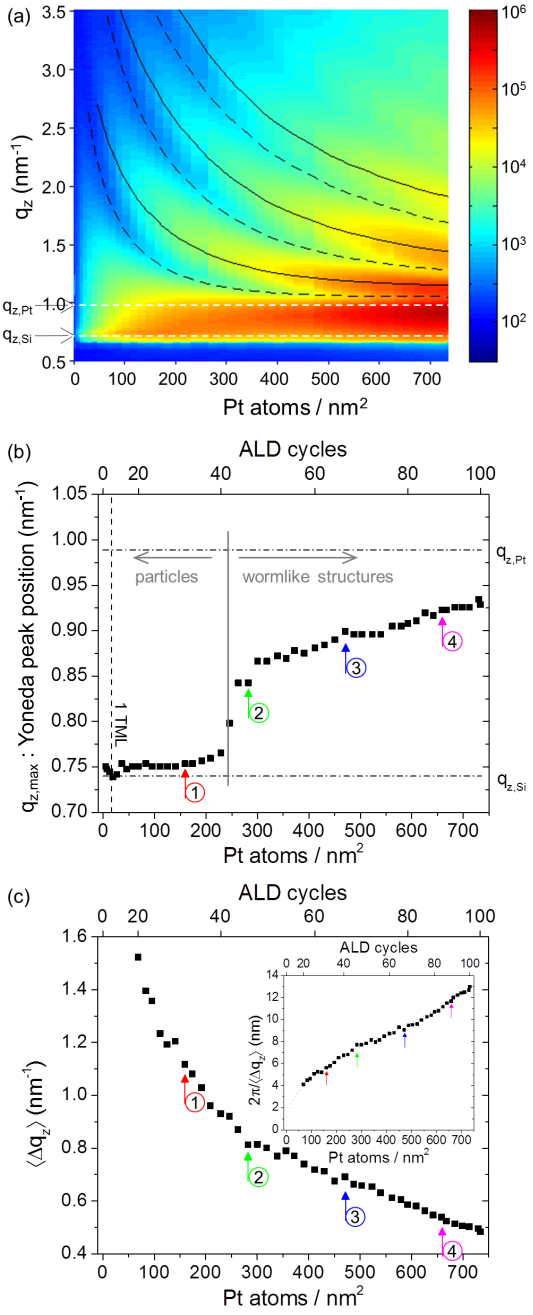

Fig. 7 (a) 2D colour map showing vertical line profiles of the main scattering peak as a function of Pt surface density. Each vertical line profile is taken at the q_y position of maximum intensity of the main scattering peak. The dashed white lines mark the Si and Pt Yoneda positions. The solid and dashed black lines indicate the evolution of the higher order maxima and minima, respectively. (b) Position of the q_z maximum of the main scattering peak as a function of ALD cycles and Pt surface density. (c) Average distance between two adjacent maxima and/or minima, $< q_z >$, versus ALD cycles and Pt surface density. The inset shows the corresponding values for $2\pi/ < \Delta q_z >$. The coloured numbers and arrows (1-4) refer to the data/SEM micrographs in Figure 3.

View Article Online
DOI: 10.1039/D0CP03563G

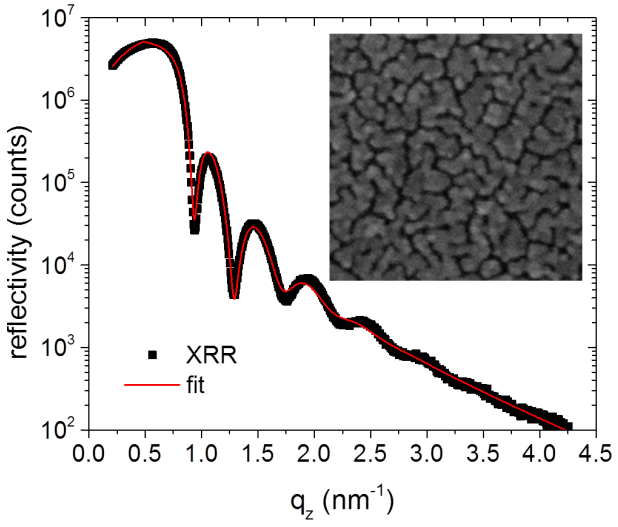

Fig. 8 *Ex situ* characterization after 100 cycles of Pt ALD. X-ray reflectivity pattern with fit to the data, the fitted thickness is equal to 12.1 nm. The SEM image has a width of 500 nm.

the H, and R values (Figure 9c, black triangles) are determined from the GISAXS pattern using the "fast" data analysis and the following relation is used to determine the center-to-center distance D:

$$D = \sqrt{\frac{2}{3}\pi R^2 H \frac{66.24 \text{ atoms} / \text{nm}^3}{S_{Pt}}} \quad (1)$$

with S_{Pt} the Pt surface density and 66.24 being the number of Pt atoms that are present in a cubic nm of bulk Pt. As will be discussed in the next section, simulation results (open red symbols in Figure 9) confirm that this approach is more reliable than the common approach of using the approximation $D = 2\pi/q_{y,max}$ to estimate the center-to-center distance. Note that Figure 9c suggests that the initial nuclei have an aspect ratio close to 1:1, marked by a similar mean particle width and height. With increasing Pt loading, the mean particle width increases faster than the mean particle height, pointing towards lateral growth of the nanoparticles, giving rise to laterally elongated particles.

3.4.2 Simulation of GISAXS patterns

The purpose of the simple geometrical model is to quickly extract parameters for the average particle height, radius, and interparticle distance from the quasi real time feedback of the particle morphology during the experiments. However, validation of this model is required by simulating full 2D GISAXS patterns and demonstrating that good agreement is achieved with the experimental patterns. In the next paragraphs we describe a step-by-step approach that we applied to model the nanoparticle shape, dimensions, and spacing and obtain reasonable agreement between data and simulation (see Supporting Information for a schematic representation of the analysis approach). The parameters extracted from the simplified geometrical model (full black symbols in Figure 9b-d, with values for D determined by Eq. 1) served as initial input parameters for the simulations, which required only slight optimization during the simulation procedure, yielding the data depicted by the open red symbols in Figure 9b-d as the simulation output. The optimized H and R values only differ slightly from the initial input parameters, while the optimized average center-to-center distance D does not differ much from its initial input value. This provides a good indication that the proposed geometrical model is a physically relevant model that yields valuable information on the evolution of the average particle height, radius and center-to-center distance during the ALD process, without the complexity of a full 2D GISAXS simulation.

The optimization of the initial input values is illustrated in Figure 10. It shows the experimental (black data points) and simulated (red curves) line profiles of the GISAXS patterns recorded at 22, 32, and 42 ALD cycles. The line profiles for 12 ALD cycles can be found in the Supporting Information. The form factor was calculated for full spheroids without size distributions. The interference function was described by the mean correlation length D and a Gaussian distribution function with disorder parameter ω. The shape of the main scattering peak in the horizontal line profiles was found to be well reproduced for an ω value equal to 0.4 D. Simulations with the initial average H, R and D values extracted from the geometrical model yielded the dashed red curves as output. The obtained curves are able to decently reproduce the maxima and minima of the horizontal line profiles (top panels), although their q_y positions are slightly underestimated. For the vertical line profiles (bottom panels), it is only possible to reproduce the first profile (a), for the other profiles the number of minima and maxima is reproduced but their position is shifted to higher q_z values, indicating that the input underestimates the height of the particles. Better agreement can be obtained after optimizing the initial H, R, and D values (solid red curves). It is clear that the used input parameters already yield a decent simulation of the line profiles and that optimizing the input values does not lead to significant changes in the relevant parameters H, R and D (Table 1).

After optimizing the main parameters (H, R, D, ω) based on 1D line profiles, the next step concerns the simulation of the entire 2D GISAXS images. During this task, it became clear that the inclusion of two particle shapes in the average form factor is needed to obtain a good reproduction of the intensity distribution of the scattering features in the 2D GISAXS patterns. For illustration, Figure 11 shows the experimental GISAXS image of ALD cycle 32 (a) together with three simulated patterns, assuming different particle shapes (b-d). The experimental pattern shows a main scattering maximum with several secondary scattering features along the q_z and q_y directions. In addition, there is an incomplete semi-circle present that is connecting the first secondary maxima and a diffuse background for higher q_y and q_z values. Full spheroids and half spheroids were mainly considered as possible particle shapes to describe the Pt particles, cylindrical shapes and rectangular cuboids were excluded based on the overall shape of the measured GISAXS patterns (see Supporting information). The first semi-circular shape is reproduced when full spheroids are used (Figure 11b). However, the dip in scattering intensity around $q_y = 1.0\,nm^{-1}$, $q_z = 1.5\,nm^{-1}$ is not simulated and the higher order semi-circle is too distinctly present in the simulated pattern. While the dip in scattering intensity is repro-

View Article Online
DOI: 10.1039/D0CP03563G

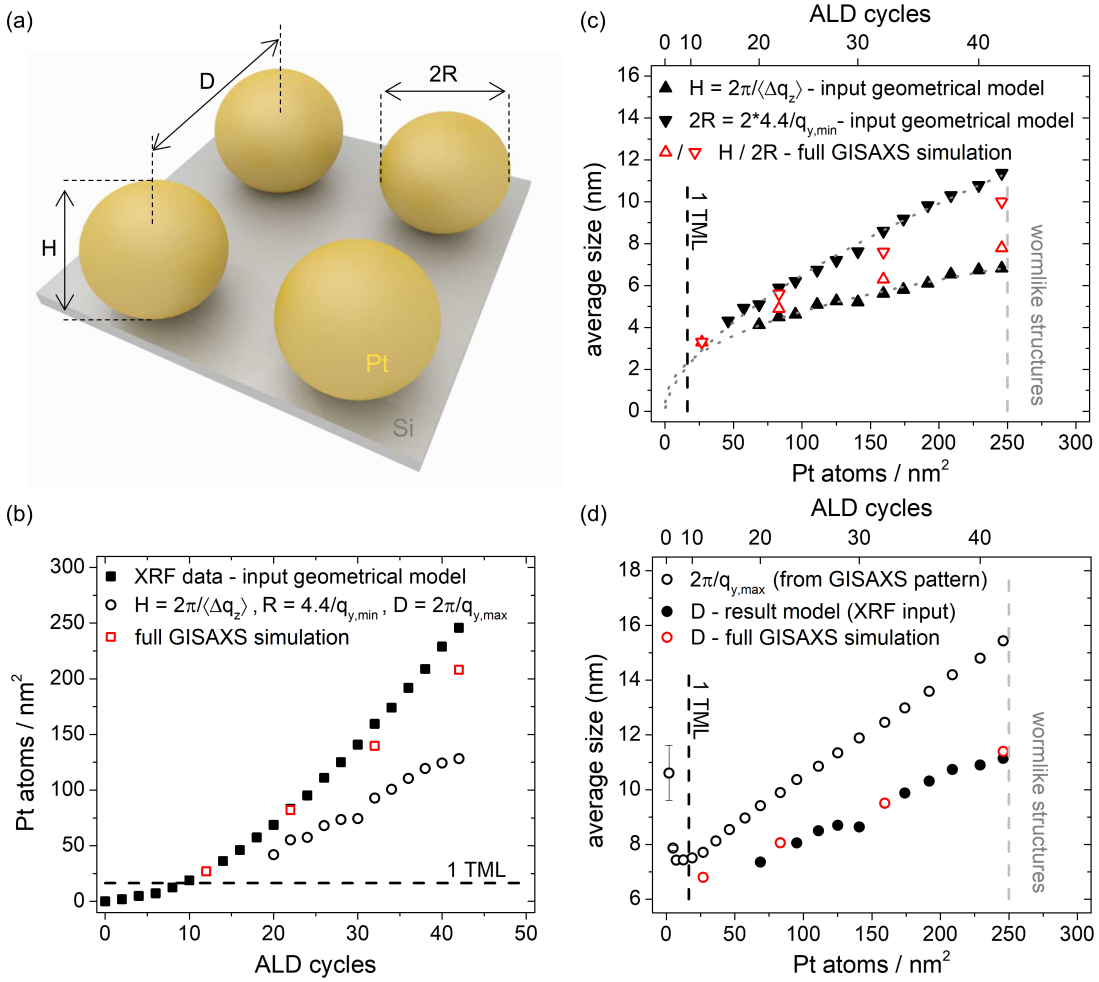

Fig. 9 (a) Schematic representation of the particle geometry and distribution, as assumed in the geometrical model for "fast analysis". (b) Pt surface density versus ALD cycles, measured by XRF (black squares), calculated from extracted H, R, and D values from "fast" GISAXS line profile analysis (circles), and extracted from "full" GISAXS simulations (open red squares). (c) Average particle height H (upward triangles) and width 2R (downward triangles) as a function of ALD cycles (top x-axis) and Pt surface density (bottom x-axis). The full black symbols are extracted from the line profile analysis and the open red symbols originate from simulations. (d) Average particle center-to-center distance D as a function of ALD cycles and Pt surface density, calculated from the proposed geometrical model (black circles) and extracted from GISAXS simulations (open red circles). The $2\pi/q_{y,max}$ values extracted from GISAXS line profiles are plotted as open black circles. The input and output values for the GISAXS simulations are displayed in Table 1.

ALD	XRF signal	Geometrical model				Optimized values from simulations				
cycle	Pt at./nm^2	H_i	$2R_i$	D_i	ω_i	H_o	$2R_o$	D_o	ω_o	Pt at./nm^2
22	83.14	4.50	5.89	8.06	3.22	4.90	5.60	8.06	3.22	82.04
32	159.42	5.62	8.60	9.51	3.80	6.30	7.60	9.51	3.80	139.55
42	245.86	6.82	11.36	11.15	4.46	7.80	10.00	11.40	4.56	208.16

Table 1 Morphological parameters used for the line profile simulations in Figure 10. H_i, $2R_i$ and D_i (in nm) were extracted from the geometrical model. The simulations used a model consisting of spheroid particles without size distribution on a regular 1D lattice with loss of long-range order described by the disorder parameter $\omega = 0.4\,D$. H_o, $2R_o$ and D_o are the optimized parameters.

View Article Online
DOI: 10.1039/D0CP03563G

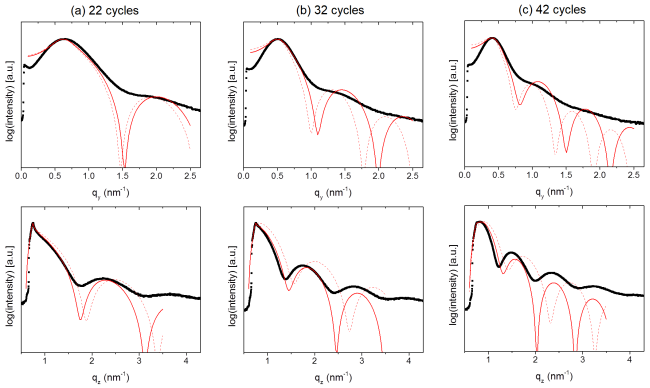

Fig. 10 Experimental (black data points) and calculated (red curves) horizontal (top) and vertical (bottom) line profiles of the GISAXS patterns obtained after 22 (a), 32 (b), and 42 (c) ALD cycles. The dashed red curves used the H, R, and D values extracted from the geometrical model as input for the calculations. The full red curves used optimized values for H, R, and D. The line profiles for 12 ALD cycles are displayed in the Supporting Information. All input parameters for the simulations are listed in Table 1.

duced when half spheroids are used as the particle shape (Figure 11d), it does not reproduce the diffuse arc-like background scattering. The best correspondence to the particular scattering features is obtained when combining both particle shapes in a 1 to 1 ratio, see Figure 11c. Both particle types are assumed to have the same average particle height and width. Therefore, both particle shapes yield the same volume per particle and this means that the previous manner to calculate D (Eq. 1) can be used to ensure that the simulated surface has the same amount of Pt as is experimentally determined from XRF.

While the main features of the GISAXS pattern are now reproduced and the introduction of two particle shapes already smooths out the line profiles, the intensity of the minima in the simulated line profiles does not fully coincide with the experimental data points, see Figure 11e-f, due to the fact that no size distribution was assumed for the Pt particles. Therefore, the complexity of the particle model is further increased by imposing size distributions on the particles to improve agreement between simulation and experiment. Good agreement is obtained by assuming a Gaussian distribution with relative width 0.05 for the particle aspect ratio H/R and a lognormal distribution for the particle radius R. The same size distributions are used for both particle shapes in the model (full spheroids and half spheroids). Simulations with variation in the radius distribution width, parameterized by the geometric standard deviation σ, are displayed in Figure 12 for the GISAXS pattern obtained after 32 ALD cycles. Figure 12a shows the experimental GISAXS pattern while (b-d) represent the simulated patterns with different radius distributions, which are depicted in the inserts. Figure 12e-f show the simulated horizontal and vertical line profiles (red curves) compared to the experimental line profiles (black data points). It is clear that using a size distribution results in further smoothing of the 1D line profiles. Based on the simulated line profiles (Figure 12e-f) the radius distribution with $\sigma = 1.05$ yields the worst fit to the experimental data and $\sigma = 1.15$ the best fit to the experimental line profiles. It is instructive to compare these particle radius distributions with the one extracted from the SEM image (Figure 3a), see Supporting Information. This comparison supports the mean R value that is obtained from the GISAXS analysis, but indicates that the distribution with a σ value of 1.30 (Figure 12d) corresponds best to the real size distribution, while its simulated line profiles do not fit as well as the simulation result using $\sigma = 1.15$ (Figure 12c). The reason for this mismatch is that there are some limitations when simulating GISAXS patterns, such as the assumption of the particle shapes and ratios between the particle shapes. In this case a one to one ratio of full and half spheroids is assumed while the real sample may have a different ratio. Nonetheless, good agreement between experiment and simulation can be achieved, without requiring large changes to the initial input parameters. This indicates that the proposed geometrical model can be used for a quantitative assessment of the 2D GISAXS images that are obtained during the Pt ALD process.

3.5 Effect of precursor dose on the Pt nucleation

The previous sections provided the reader insights into how *in situ* recorded XRF signals and scattering patterns, in particular the q positions of the minima and maxima in the patterns and line profiles, can provide information on the morphological parameters during the ALD process. In this part of the manuscript, the *in situ* XRF and GISAXS methodology is used to study the influence of the precursor dosing on the Pt nucleation and island growth mode. Generally, in the steady growth regime of ALD processes the surface reactions are in saturation, provided that a sufficiently large precursor dose is applied, which is determined from saturation experiments. Using a precursor exposure that is larger than the saturation exposure has no effect on the growth, instead it results in waste of the excess precursor. However, surface reactions of a different nature are taking place during the nucleation and island growth regime, and the precursor dose obtained from typical steady growth saturation experiments may not lead to saturation of these initial surface reactions. As a result, increasing the precursor exposure beyond the point of saturation for steady growth can have an influence on the growth and deposition rate (number of Pt atoms deposited per cycle),[5] motivating the study presented below.

Two experiments were performed, using either a pump mode or static mode precursor exposure. During pump mode the ALD chamber is actively pumped during the precursor exposure and the pressure (precursor and argon) in the chamber reaches 6×10^{-3} mbar. To perform an exposure in static mode, the valve between the ALD chamber and turbomolecular pump needs to be closed. This is followed by precursor injection, until the pressure (precursor and argon) in the chamber reaches 1 mbar. It should be noted that both these precursor doses yield saturated growth in the steady regime, as verified by saturation experiments on sputtered Pt thin films.[69,70] The Pt surface density as a function of the number of ALD cycles for these experiments is displayed in Figure 13a. As seen in the zoom of the first 25 ALD cycles (Figure 13b) the static mode results in a higher deposition rate (number of Pt atoms per cycle) during the nucleation regime than

View Article Online
DOI: 10.1039/D0CP03563G

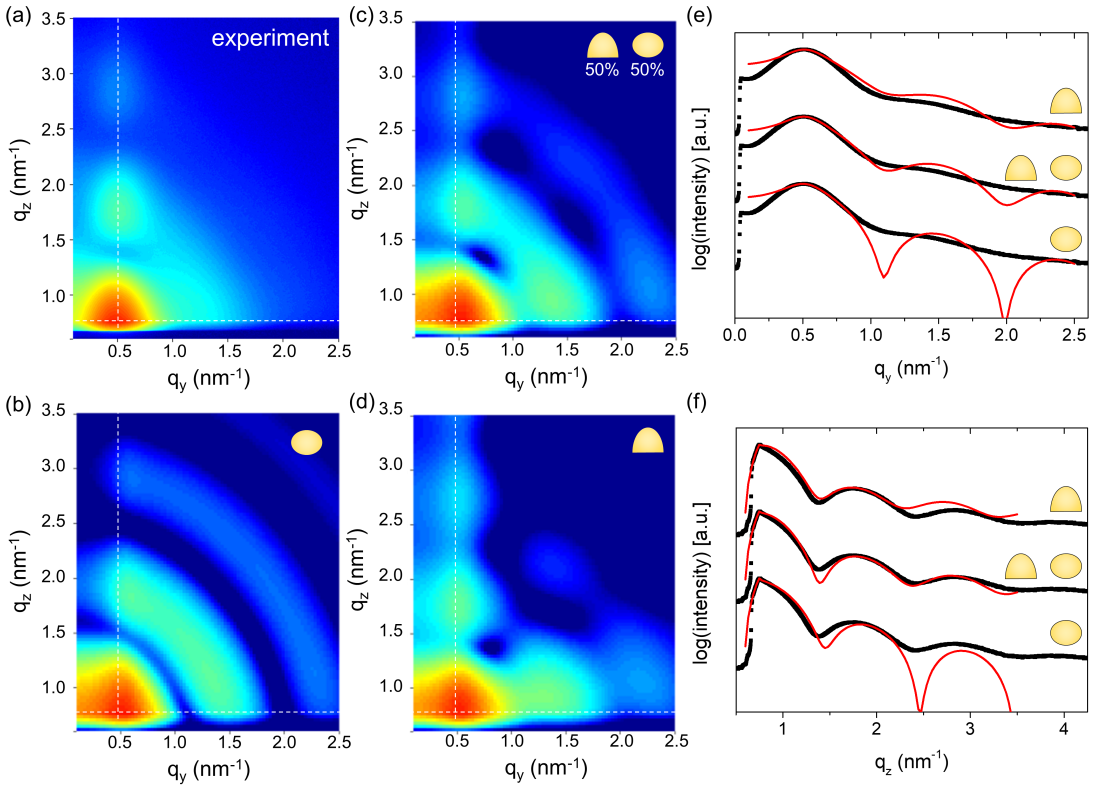

Fig. 11 Experimental (a) and simulated (b-d) 2D GISAXS patterns, obtained at 32 ALD cycles. The assumed particle shapes for the calculations are schematically represented in the top right corner of the images. Horizontal (e) and vertical (f) line profiles of the experimental (black data points) and calculated (red curves) GISAXS patterns. The profiles were given an offset for clarity. The morphological parameters used for the simulations were extracted from the optimized line profile simulations in Figure 10: $H_0 = 6.30$ nm, $2R_0 = 7.60$ nm, $D_0 = 9.51$ nm, $\omega_o = 3.80$. No size distributions are taken into account.

View Article Online
DOI: 10.1039/D0CP03563G

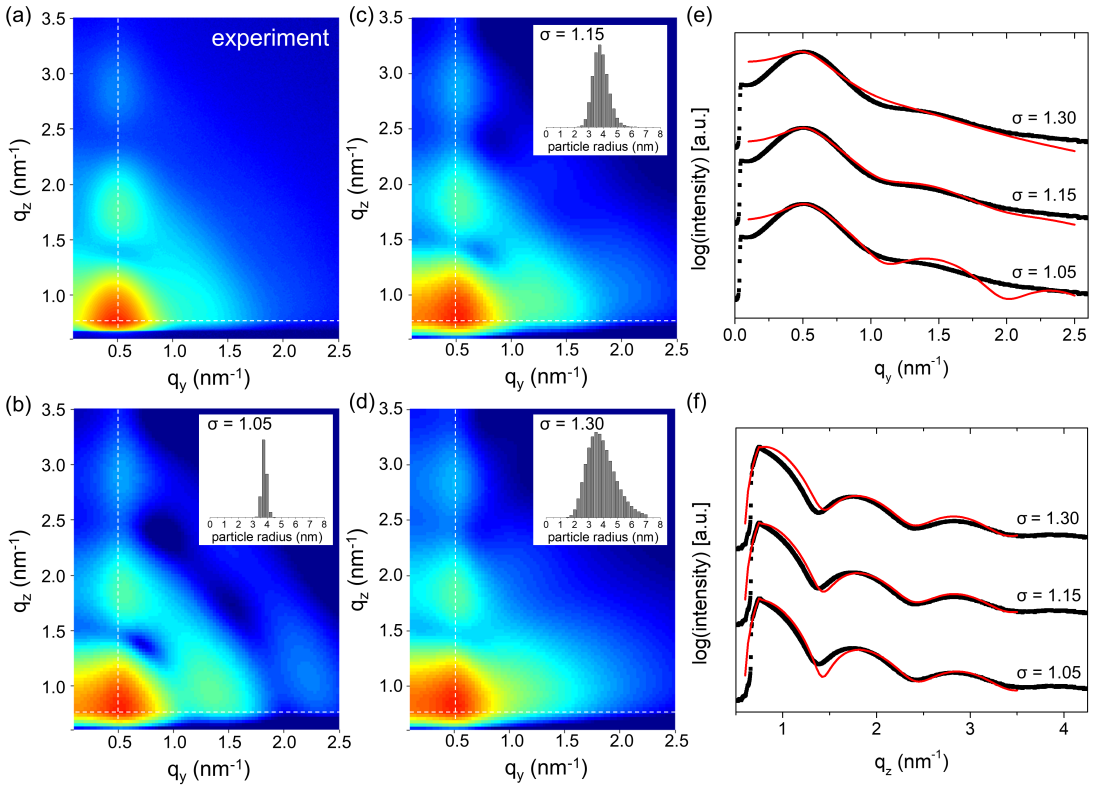

Fig. 12 Experimental (a) and calculated (b-d) 2D GISAXS patterns, obtained at 32 ALD cycles. The particle radius distributions are varied for the simulated patterns and are represented in the top right corner of the images. Horizontal (e) and vertical (f) line profiles of the experimental (black data points) and calculated (red curves) GISAXS patterns. The profiles were given an offset for clarity. The morphological parameters used for the simulations were extracted from the optimized line profile simulations in Figure 10: $H_0 = 6.30$ nm, $2R_0 = 7.60$ nm, $D_0 = 9.51$ nm, $\omega_o = 3.80$.

the use of pump mode exposures. For larger Pt loadings, the XRF curves follow the same trend, so the deposition rate becomes similar. To investigate whether the precursor dosing mode only has an effect on the amount of Pt that is deposited per cycle during the formation of the initial nuclei or also during the coalescence and growth stage, a mixed experiment (green triangles) was performed during which the first 4 ALD cycles used static mode precursor exposures and the following cycles used pump mode precursor exposures. In this combination experiment the nucleation occurs faster due to the first 4 ALD cycles that use static exposures modes. However, after these initial cycles the amount of Pt atoms that is deposited per cycle is lower than for the purely static mode experiment. Thus the effect of the used precursor exposure on the Pt deposition per cycle extends further than these first 4 ALD cycles.

The difference in nucleation behaviour between static and pump mode might also induce a difference in morphology of the Pt particles on the surface. As the GISAXS patterns reflect the specific morphology on the surface, comparing them for the different exposure experiments will highlight the differences in morphology of the Pt particles. Comparing the different experiments as a function of ALD cycles leads to different GISAXS patterns for all experiments (see Supporting Information), which is to be expected since the same number of ALD cycles will not lead to similar Pt loadings for the different experiments. Therefore, it is more relevant to compare the GISAXS patterns of the three experiments for similar Pt surface densities, see Figure 14. Each row represents a different experiment and the columns show patterns that represent similar Pt surface densities on the surface for the three experiments. The vertical and horizontal line profiles of these GISAXS patterns can be found in the Supporting Information. From these GISAXS patterns and line profiles it is clear that a similar Pt loading leads to a similar scattering pattern, regardless of the used exposure mode. This is a clear indication that the surface morphology is not significantly influenced by the deposition rate and the exposure mode that is used during the process. This observation can be linked to the effect of surface mobility that plays an important role on the morphology of the Pt particles that are formed on the surface. As highlighted before, the GISAXS pattern sequence clearly shows a continuous shift of the main scattering peak towards lower q_y values during the Pt depositions. This shift can only be explained by a continuous diffusion-driven coalescence.[40,48] Remarkably, it seems that during the deposition at a substrate temperature of 300 °C and for an O_2-based reactant the particle morphology is dominated by surface diffusion and completely determined by the loading. Further tuning of the morphology is possible by post-deposition annealing,[59] which causes sintering of the particles, or using another co-reactant during the deposition.[12]

View Article Online
DOI: 10.1039/D0CP03563G

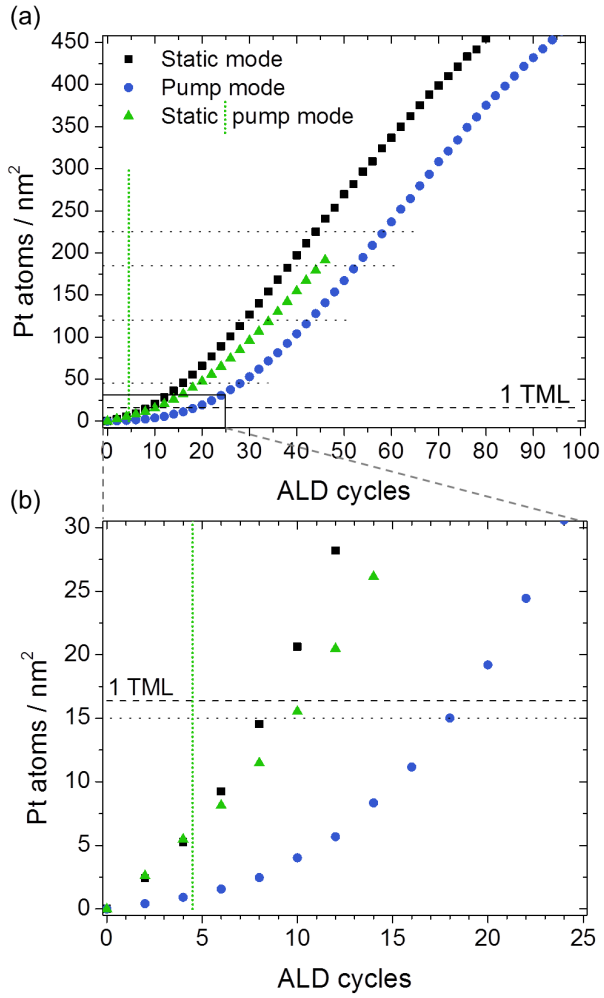

Fig. 13 (a) Pt surface density as a function of ALD cycles for three experiments using different Pt precursor dose modes. RBS was used to calibrate the *in situ* XRF data. (b) Detail of the nucleation stage. The dotted horizontal lines correspond to the Pt loadings for which the *in situ* GISAXS patterns are shown in Figure 14

4 Discussion

4.1 Particle nucleation

Information about the behaviour of the Pt particles during the nucleation stage can be obtained by analysing the evolution of the main scattering peak during the initial ALD cycles. A theoretical monolayer of Pt is only obtained after 10 ALD cycles. During these initial ALD cycles the resulting GISAXS pattern does not exhibit secondary maxima and minima for the observable reciprocal q-space, which makes it very difficult to accurately obtain a value for the average particle height and radius. While the center-to-center distance estimated from the relation $D = 2\pi/q_{y,max}$ overestimates the distance, though only slightly for low Pt loadings (see simulation for 12 ALD cycles in Figure 9), the evolution of the main scattering lobe can still provide information about the particles that are deposited. After the main scattering peak appears it shifts to higher q_y values during the first 6 ALD cycles, indicating a decrease of the mean particle distance and an increase in the number of deposited nuclei on the surface. This is followed by a shift to lower q_y values after the 6th ALD cycle, indicating that there is a critical or saturated particle coverage that cannot be exceeded. The data gives an estimated saturated particle density of $N \sim 1.8 \times 10^{12}$ nuclei/cm^2 after 6 ALD cycles, which is followed by an increase in the center-to-center distance indicating a reduction in the number of scattering nuclei due to coalescence. After the saturated coverage is achieved small clusters will rather fuse with existing islands instead of forming new stable nuclei. At the end of the nucleation stage, at ca. 12 ALD cycles, the analysis yields Pt clusters of a size of ca. 3 nm with an aspect ratio of 1:1 and a center-to-center spacing of ca. 7 nm.

4.2 Particle growth and coalescence

After reaching the saturated particle coverage the main scattering peak keeps shifting towards lower q_y and higher q_z values with every GISAXS measurement and secondary maxima and minima start to appear, which can be used to estimate the particle radius and particle height. The appearance of secondary maxima and minima on the main scattering peak and their shift to lower q_z values correlates to an increase of the particle height with every ALD cycle. The shift in q_y of the main lobe indicates that the center-to-center distance increases with every ALD cycle, which is also obtained from the geometrical model (Figure 9d). The evolution of the horizontal secondary maxima and minima indicates that the radius of the particles increases with every ALD cycle and it seems that the particle width increases faster than the particle height. All this is consistent with the growth and coalescence of the Pt nanoparticles. Generally, one can distinguish two main coalescence mechanisms, a static and a dynamic coalescence mechanism.[37,71–73] A static coalescence mechanism means that the formed nuclei grow until neighbouring islands start to touch, which leads to merging of the islands into a larger particle geometry. On the other hand, dynamic coalescence involves the diffusion and adsorption of adatom clusters or small particles, and can result in a laterally elongated particle geometry when the supply of material from the gas phase is smaller than the supply via migrating surface species and clusters.[48] The *in situ* GISAXS data

View Article Online
DOI: 10.1039/D0CP03563G

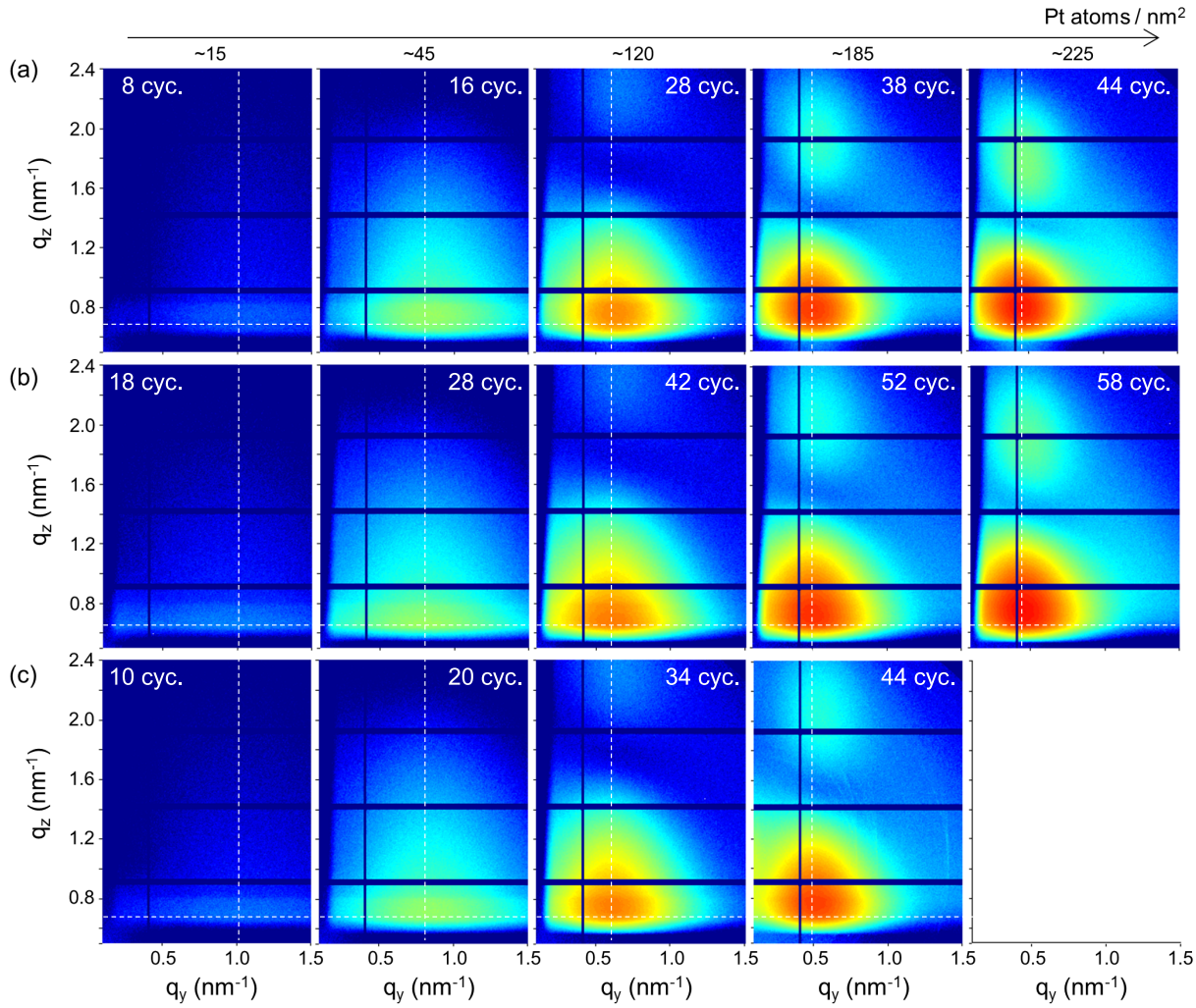

Fig. 14 *In situ* measured 2D GISAXS patterns for Pt surface densities of ~ 15, ~ 45, ~ 120, ~ 185, ~ 225 Pt atoms per nm^2 during three experiments, using different Pt precursor dose modes: (a) static mode, (b) pump mode, and (c) static mode during the first 4 ALD cycles, followed by pump mode. The number of performed ALD cycles to obtain the GISAXS pattern is labelled in every pattern. Horizontal and vertical cuts of these patterns are compared in the Supporting Information.

View Article Online
DOI: 10.1039/D0CP03563G

indicate that the Pt ALD process using O_2 as a co-reactant is governed by a dynamic growth and coalescence mechanism. The end of the nucleation stage – where the model yields ca. 3 nm wide Pt islands at a center-to-center spacing of ca. 7 nm, leaving a gap of ca. 4 nm between neighboring particles – is immediately followed by a continuous increase in center-to-center distance and hence a decrease in particle areal density. This can only be explained by diffusion-driven particle coalescence. Hence, our *in situ* GISAXS and XRF method provides a powerful way to probe surface mobility during the nucleation and island growth stages of ALD processes and distinguish between static and dynamic particle growth and coalescence. Finally, as more Pt is added to the surface the q_z position of maximum scattering intensity shifts to larger values, towards the expected value of a Pt surface, due to the increase of the average density of the scattering volume. This shift in q_z exhibits a rapid increase around a surface density of 250 Pt atoms per nm^2 and based on the *ex situ* SEM micrographs (Figure 3b) it coincides with a change in the morphology of the Pt particles, transitioning from spherical shapes to more worm-like particle shapes. Once these worm-like features appear the Pt particles can no longer be approximated by spherical shapes and the geometrical model is no longer used as more complex particle shapes need to be assumed.

4.3 Influence of precursor dose

The standard precursor exposure mode in this work made use of a high-exposure static pulse, which reached a pressure of 1 mbar during the exposure. The influence of a low exposure mode, in pump mode with a pressure of 6×10^{-3} mbar, was also investigated to study its influence on the nucleation and island growth behaviour of the ALD process. The higher exposure leads to faster nucleation of the Pt nanoparticles, which is seen by the need of 20 ALD cycles to reach a theoretical monolayer of Pt with the low exposure mode compared to 10 ALD cycles for the high exposure mode. However, once the nucleation stage has ended both high and low exposure modes lead to a similar growth curve, indicating that the difference for both exposure modes is mainly related to the nucleation process. The combined exposure mode experiment shows that this nucleation stage extends beyond the first 4 ALD cycles, because the growth curve after the initial 4 cycles in this experiment starts to deviate from the purely high exposure mode experiment. Next to its effect on the nucleation speed, the use of different exposure modes might also influence the final morphology of the deposited Pt particles. However, matching the GISAXS patterns with similar Pt loadings from the different experiments shows that a similar Pt loading results in a similar scattering pattern and therefore a similar particle morphology on the surface. The surface mobility of the Pt atoms seems to drive the particles to a certain morphology, which depends on the Pt surface density. Therefore, at a substrate temperature of 300 °C and using oxygen as the co-reactant an important parameter to tune the morphology of the Pt particles is the loading.

5 Conclusions

We investigated the nucleation and growth behaviour of Pt ALD on planar SiO_2 substrates by combining *in situ* XRF and GISAXS measurements. A simple geometrical model and fast analysis approach of the 2D GISAXS patterns was used and its validity was verified by simulating the model with the IsGISAXS software and comparing the results to the experimentally obtained scattering patterns. This showed that the geometrical model and initial input parameters obtained from the fast analysis provide a good description of the Pt nanoparticles during the ALD process, before they start coalescing in irregular shapes.

Analysis of the 2D GISAXS patterns during the nucleation stage indicates that in the initial stage new nuclei are formed until a critical coverage is reached after 6 ALD cycles, estimated to be $N\sim1.8\times10^{12}$ nuclei/cm^2 which is in agreement with expected values from literature. Additional ALD cycles lead to an increase in the center-to-center distance of the particles, indicating a reduction in the number of scattering nuclei due to diffusion-driven coalescence. After this point the center-to-center distance keeps increasing, as does the particle radius and height. For a coverage above 250 Pt atoms per nm^2 the *ex situ* SEM micrographs reveal that the Pt particles coalesce into irregular shapes, which coincides with an abrupt increase of the q_z position of the scattering maximum in the 2D GISAXS pattern towards the expected q_z position of a pure Pt surface.

Finally, the effect of a lower precursor exposure during the ALD process is investigated. Using a lower precursor exposure results in a remarkably slower nucleation process. However, once the nucleation process is finished both precursor exposures lead to similar slopes in the growth curves. It was found that while using a larger precursor exposure leads to remarkably faster nucleation it does not influence the particle morphology, instead the morphology is determined by the Pt surface density that is reached when oxygen is used as the co-reactant. These results prove that combining *in situ* GISAXS and XRF measurements provides an excellent experimental strategy to obtain new fundamental insights of the role of deposition parameters on the morphology of Pt ALD depositions.

Conflicts of interest

There are no conflicts to declare.

Acknowledgement

This research was funded by the Research Foundation – Flanders (FWO) and the Special Research Fund BOF of Ghent University (GOA 01G01019). J. D., R. K. R. and M. M. M. acknowledge the FWO for a research fellowship. For the GISAXS and XRF measurements, the authors received funding from the European Community's Trans National Access Program CALIPSO. We are also grateful to the SOLEIL and ESRF staff for smoothly running the facilities. The authors thank Prof. A. Vantomme for RBS measurements.

View Article Online
DOI: 10.1039/D0CP03563G

Notes and references

1 J. Hämäläinen, M. Ritala and M. Leskelä, *Chemistry of Materials*, 2014, **26**, 786–801.

2 C. Detavernier, J. Dendooven, S. Pulinthanathu Sree, K. F. Ludwig and J. A. Martens, *Chem. Soc. Rev.*, 2011, **40**, 5242–5253.

3 V. Cremers, R. L. Puurunen and J. Dendooven, *Applied Physics Reviews*, 2019, **6**, 021302.

4 B. J. O'Neill, D. H. K. Jackson, J. Lee, C. Canlas, P. C. Stair, C. L. Marshall, J. W. Elam, T. F. Kuech, J. A. Dumesic and G. W. Huber, *ACS Catalysis*, 2015, **5**, 1804–1825.

5 A. J. M. Mackus, M. J. Weber, N. F. W. Thissen, D. Garcia-Alonso, R. H. J. Vervuurt, S. Assali, A. A. Bol, M. A. Verheijen and W. M. M. Kessels, *Nanotechnology*, 2015, **27**, 034001.

6 J. Lu, J. W. Elam and P. C. Stair, *Surface Science Reports*, 2016, **71**, 410 – 472.

7 R. K. Ramachandran, C. Detavernier and J. Dendooven, in *Atomic Layer Deposition for Catalysis*, John Wiley & Sons, Ltd, 2017, ch. 14, pp. 335–358.

8 H.-B.-R. Lee, M. N. Mullings, X. Jiang, B. M. Clemens and S. F. Bent, *Chemistry of Materials*, 2012, **24**, 4051–4059.

9 J. Lu, J. W. Elam and P. C. Stair, *Accounts of Chemical Research*, 2013, **46**, 1806–1815.

10 Y. Lei, J. Lu, X. Luo, T. Wu, P. Du, X. Zhang, Y. Ren, J. Wen, D. J. Miller, J. T. Miller, Y.-K. Sun, J. W. Elam and K. Amine, *Nano Letters*, 2013, **13**, 4182–4189.

11 M. Filez, H. Poelman, R. K. Ramachandran, J. Dendooven, K. Devloo-Casier, E. Fonda, C. Detavernier and G. B. Marin, *Catalysis Today*, 2014, **229**, 2 – 13.

12 J. Dendooven, R. K. Ramachandran, E. Solano, M. Kurttepeli, L. Geerts, G. Heremans, J. Rongé, M. M. Minjauw, T. Dobbelaere, K. Devloo-Casier, J. A. Martens, A. Vantomme, S. Bals, G. Portale, A. Coati and C. Detavernier, *Nature Communications*, 2017, 1074.

13 C. Wang, L. Hu, K. Poeppelmeier, P. C. Stair and L. Marks, *Nanotechnology*, 2017, **28**, 185704.

14 C. Wang, L. Hu, Y. Lin, K. Poeppelmeier, P. Stair and L. Marks, *Journal of Physics D: Applied Physics*, 2017, **50**, 415301.

15 M. J. Weber, A. J. M. Mackus, M. A. Verheijen, C. van der Marel and W. M. M. Kessels, *Chemistry of Materials*, 2012, **24**, 2973–2977.

16 J. Lu, K.-B. Low, Y. Lei, J. A. Libera, P. C. Nicholls, Alanand Stair and J. W. Elam, *Nature Communications*, 2014, **5**, 3264.

17 J. A. Singh, N. F. W. Thissen, W.-H. Kim, H. Johnson, W. M. M. Kessels, A. A. Bol, S. F. Bent and A. J. M. Mackus, *Chemistry of Materials*, 2018, **30**, 663–670.

18 M. J. Weber, M. A. Verheijen, A. A. Bol and W. M. M. Kessels, *Nanotechnology*, 2015, **26**, 094002.

19 K. Cao, Q. Zhu, B. Shan and R. Chen, *Scientific Reports*, 2010, **5**, 8470.

20 S. T. Christensen, H. Feng, J. L. Libera, N. Guo, J. T. Miller, P. C. Stair and J. W. Elam, *Nano Letters*, 2010, **10**, 3047–3051.

21 A. J. M. Mackus, S. A. F. Dielissen, J. J. L. Mulders and W. M. M. Kessels, *Nanoscale*, 2012, **4**, 4477–4480.

22 M. M. Minjauw, H. Rijckaert, I. V. Driessche, C. Detavernier and J. Dendooven, *Chemistry of Materials*, 2019, **31**, 1491–1499.

23 D. N. Goldstein and S. M. George, *Applied Physics Letters*, 2009, **95**, 143106.

24 Y. Hwang, B.-M. Nguyen and S. A. Dayeh, *Applied Physics Letters*, 2013, **103**, 263115.

25 A. A. Dameron, S. Pylypenko, J. B. Bult, K. Neyerlin, C. Engtrakul, C. Bochert, G. J. Leong, S. L. Frisco, L. Simpson, H. N. Dinh and B. Pivovar, *Applied Surface Science*, 2012, **258**, 5212 – 5221.

26 C. de Paula, N. E. Richey, L. Zeng and S. F. Bent, *Chemistry of Materials*, 2020, **32**, 315–325.

27 S. T. Christensen, J. W. Elam, B. Lee, Z. Feng, M. J. Bedzyk and M. C. Hersam, *Chemistry of Materials*, 2009, **21**, 516–521.

28 A. J. M. Mackus, M. A. Verheijen, N. Leick, A. A. Bol and W. M. M. Kessels, *Chemistry of Materials*, 2013, **25**, 1905–1911.

29 F. Grillo, H. Van Bui, J. A. Moulijn, M. T. Kreutzer and J. R. van Ommen, *The Journal of Physical Chemistry Letters*, 2017, **8**, 975–983.

30 F. Grillo, J. A. Moulijn, M. T. Kreutzer and J. R. van Ommen, *Catalysis Today*, 2018, **316**, 51 – 61.

31 N. E. Richey, C. de Paula and S. F. Bent, *The Journal of Chemical Physics*, 2020, **152**, 040902.

32 D. Goldstein and S. George, *Thin Solid Films*, 2011, **519**, 5339 – 5347.

33 A. J. M. Mackus, N. Leick, L. Baker and W. M. M. Kessels, *Chemistry of Materials*, 2012, **24**, 1752–1761.

34 W. Setthapun, W. D. Williams, S. M. Kim, H. Feng, J. W. Elam, F. A. Rabuffetti, K. R. Poeppelmeier, P. C. Stair, E. A. Stach, F. H. Ribeiro, J. T. Miller and C. L. Marshall, *The Journal of Physical Chemistry C*, 2010, **114**, 9758–9771.

35 X. Liang, Y. Zhou, J. Li and A. W. Weimer, *Journal of Nanoparticle Research*, 2011, **13**, 3781–3788.

36 T. D. Gould, A. M. Lubers, A. R. Corpuz, A. W. Weimer, J. L. Falconer and J. W. Medlin, *ACS Catalysis*, 2015, **5**, 1344–1352.

37 G. Renaud, R. Lazzari and F. Leroy, *Surface Science Reports*, 2009, **64**, 255 – 380.

38 D. Babonneau, S. Camelio, E. Vandenhecke, S. Rousselet, M. Garel, F. Pailloux and P. Boesecke, *Phys. Rev. B*, 2012, **85**, 235415.

39 J. R. Levine, J. Cohen and Y. Chung, *Surface Science*, 1991, **248**, 215 – 224.

40 G. Renaud, R. Lazzari, C. Revenant, A. Barbier, M. Noblet, O. Ulrich, F. Leroy, J. Jupille, Y. Borensztein, C. R. Henry, J.-P. Deville, F. Scheurer, J. Mane-Mane and O. Fruchart, *Science*, 2003, **300**, 1416–1419.

41 M. H. Kim, B. Lee, S. Lee, C. Larson, J. M. Baik, C. T. Yavuz, S. Seifert, S. Vajda, R. E. Winans, M. Moskovits, G. D. Stucky and A. M. Wodtke, *Nano Letters*, 2009, **9**, 4138–4146.

42 L. i. m. c. Arslan, C. Sanborn, E. Anzenberg and K. F. Ludwig,

View Article Online
DOI: 10.1039/D0CP03563G

Phys. Rev. Lett., 2012, **109**, 106102.

43 A. Demasi, M. G. Rainville and K. F. Ludwig, *Journal of Vacuum Science & Technology A*, 2015, **33**, 021406.

44 R. Lazzari, F. Leroy and G. Renaud, *Phys. Rev. B*, 2007, **76**, 125411.

45 J. Olander, R. Lazzari, J. Jupille, B. Mangili, J. Goniakowski and G. Renaud, *Phys. Rev. B*, 2007, **76**, 075409.

46 R. Lazzari, G. Renaud, C. Revenant, J. Jupille and Y. Borensztein, *Phys. Rev. B*, 2009, **79**, 125428.

47 G. Kaune, M. A. Ruderer, E. Metwalli, W. Wang, S. Couet, K. Schlage, R. Röhlsberger, S. V. Roth and P. Müller-Buschbaum, *ACS Applied Materials & Interfaces*, 2009, **1**, 353–360.

48 M. Schwartzkopf, A. Buffet, V. Körstgens, E. Metwalli, K. Schlage, G. Benecke, J. Perlich, M. Rawolle, A. Rothkirch, B. Heidmann, G. Herzog, P. Müller-Buschbaum, R. Röhlsberger, R. Gehrke, N. Stribeck and S. V. Roth, *Nanoscale*, 2013, **5**, 5053–5062.

49 G. Santoro, S. Yu, M. Schwartzkopf, P. Zhang, S. Koyiloth Vayalil, J. F. H. Risch, M. A. Rübhausen, M. Hernández, C. Domingo and S. V. Roth, *Applied Physics Letters*, 2014, **104**, 243107.

50 S. Yu, G. Santoro, Y. Yao, D. Babonneau, M. Schwartzkopf, P. Zhang, S. K. Vayalil, P. Wessels, R. Döhrmann, M. Drescher, P. Müller-Buschbaum and S. V. Roth, *The Journal of Physical Chemistry C*, 2015, **119**, 4406–4413.

51 K. Devloo-Casier, J. Dendooven, K. F. Ludwig, G. Lekens, J. D'Haen and C. Detavernier, *Applied Physics Letters*, 2011, **98**, 231905.

52 V. R. Anderson, N. Nepal, S. D. Johnson, Z. R. Robinson, A. Nath, A. C. Kozen, S. B. Qadri, A. DeMasi, J. K. Hite, K. F. Ludwig and C. R. Eddy, *Journal of Vacuum Science & Technology A*, 2017, **35**, 031508.

53 N. Nepal, V. R. Anderson, S. D. Johnson, B. P. Downey, D. J. Meyer, A. DeMasi, Z. R. Robinson, K. F. Ludwig and C. R. Eddy, *Journal of Vacuum Science & Technology A*, 2017, **35**, 031504.

54 J. M. Woodward, S. G. Rosenberg, A. C. Kozen, N. Nepal, S. D. Johnson, C. Wagenbach, A. H. Rowley, Z. R. Robinson, H. Joress, K. F. Ludwig and C. R. Eddy, *Journal of Vacuum Science & Technology A*, 2019, **37**, 030901.

55 N. Nepal, V. R. Anderson, S. D. Johnson, B. P. Downey, D. J. Meyer, Z. R. Robinson, J. M. Woodward, K. F. Ludwig and C. R. Eddy, *Journal of Vacuum Science & Technology A*, 2019, **37**, 020910.

56 J. Dendooven, E. Solano, M. M. Minjauw, K. Van de Kerckhove, A. Coati, E. Fonda, G. Portale, Y. Garreau and C. Detavernier, *Review of Scientific Instruments*, 2016, **87**, 113905.

57 J. Dendooven, K. Devloo-Casier, M. Ide, K. Grandfield, M. Kurttepeli, K. F. Ludwig, S. Bals, P. Van Der Voort and C. Detavernier, *Nanoscale*, 2014, **6**, 14991–14998.

58 K. Devloo-Casier, P. Geiregat, K. F. Ludwig, K. van Stiphout, A. Vantomme, Z. Hens, C. Detavernier and J. Dendooven, *The Journal of Physical Chemistry C*, 2016, **120**, 18039–18045.

59 E. Solano, J. Dendooven, R. K. Ramachandran, K. Van de Kerckhove, T. Dobbelaere, D. Hermida-Merino and C. Detavernier, *Nanoscale*, 2017, **9**, 13159–13170.

60 R. K. Ramachandran, J. Dendooven, M. Filez, V. V. Galvita, H. Poelman, E. Solano, M. M. Minjauw, K. Devloo-Casier, E. Fonda, D. Hermida-Merino, W. Bras, G. B. Marin and C. Detavernier, *ACS Nano*, 2016, **10**, 8770–8777.

61 K. Devloo-Casier, K. F. Ludwig, C. Detavernier and J. Dendooven, *Journal of Vacuum Science & Technology A*, 2014, **32**, 010801.

62 S. M. Geyer, R. Methaapanon, R. Johnson, S. Brennan, M. F. Toney, B. Clemens and S. Bent, *Journal of Applied Physics*, 2014, **116**, 064905.

63 R. K. Ramachandran, M. Filez, E. Solano, H. Poelman, M. M. Minjauw, M. Van Daele, J.-Y. Feng, A. La Porta, T. Altantzis, E. Fonda, A. Coati, Y. Garreau, S. Bals, G. B. Marin, C. Detavernier and J. Dendooven, *Chemistry of Materials*, 2019, **31**, 9673–9683.

64 T. Aaltonen, M. Ritala, T. Sajavaara, J. Keinonen and M. Leskelä, *Chemistry of Materials*, 2003, **15**, 1924–1928.

65 R. Lazzari, *Journal of Applied Crystallography*, 2002, **35**, 406–421.

66 R. L. Puurunen and W. Vandervorst, *Journal of Applied Physics*, 2004, **96**, 7686–7695.

67 R. Puurunen, *Chemical Vapor Deposition*, 2004, **10**, 159–170.

68 C. T. Campbell, *Surface Science Reports*, 1997, **27**, 1 – 111.

69 D. Longrie, K. Devloo-Casier, D. Deduytsche, S. Van den Berghe, K. Driesen and C. Detavernier, *ECS Journal of Solid State Science and Technology*, 2012, **1**, Q123–Q129.

70 J. Dendooven, R. K. Ramachandran, K. Devloo-Casier, G. Rampelberg, M. Filez, H. Poelman, G. B. Marin, E. Fonda and C. Detavernier, *The Journal of Physical Chemistry C*, 2013, **117**, 20557–20561.

71 M. Zinke-Allmang, L. C. Feldman and M. H. Grabow, *Surface Science Reports*, 1992, **16**, 377 – 463.

72 P. Deltour, J.-L. Barrat and P. Jensen, *Phys. Rev. Lett.*, 1997, **78**, 4597–4600.

73 M. Zinke-Allmang, *Thin Solid Films*, 1999, **346**, 1 – 68.